Stable P3HT-PC61BM inverted organic solar cells based on cerium oxide as an electron transport layer

Sana Abidi, Amir Hossein Habibi, Hayley Melville, Sylvie Dabos-Seignon, Olivier Segut, Tony Breton, Eric Levillain, Clément Cabanetos, Saad Touihri, Philippe Blanchard

Stable P3HT-$PC_{61}BM$ inverted organic solar cells based on cerium oxide as electron transport layer

Sana Abidi,[a,b] Amir Hossein Habibi,[a] Hayley Melville,[a] Sylvie Dabos-Seignon,[a] Olivier Segut,[a] Tony Breton,[a] Eric Levillain,[a] Clément Cabanetos,[a] Saad Touihri,[b*] and Philippe Blanchard[a*]

[a] Univ Angers, CNRS, MOLTECH-ANJOU, SFR MATRIX, F-49000 Angers, France.
[b] Laboratoire Nanomatériaux, Nanotechnologie et Energie (L2NE), University of Tunis el Manar, Tunisia.

Corresponding authors: philippe.blanchard@univ-angers.fr; saad.touihri@ensit.rnu.tn

Abstract

The potential of cerium oxide (CeO_x) as electron transport layer (ETL) was explored in inverted bulk heterojunction organic solar cells (BHJ OSCs), using a mixture of P3HT and $PC_{61}BM$ as photoactive layer, and compared with the benchmark zinc oxide (ZnO). CeO_x layers on indium tin oxide or glass were obtained by spin-coating a solution prepared from $Ce(OAc)_3.yH_2O$ followed by thermal annealing which was optimized. CeO_x layers were characterized by different analytical techniques such as X-ray photoelectron spectroscopy showing that thermal annealing at 200°C for 15 minutes led to the formation of CeO_x, with a value of x reaching 1.70. These optimized thin layers of CeO_x were successfully used as ETL in P3HT-$PC_{61}BM$ inverted OSCs exhibiting power conversion efficiencies (PCEs) reaching 1.7% whereas ZnO-based devices showed a maximum PCE of 3.2%. Although annealing at 450°C led to CeO_x layers with a higher x value of 1.79, the PCEs of the devices became significantly lower due to the appearance of large crystalline clusters in the CeO_x layer, as shown by AFM, likely producing short circuits. ZnO thin films doped with 3 mol % of CeO_x were tested leading to a slight decrease of the photovoltaic efficiency. Importantly, the efficiency of the CeO_x-based OSCs increased up to 2.1% after two weeks and remained higher than the initial value after one month, while OSCs based on ZnO doped with CeO_x retained 85% of its initial PCE after five month's storage. These results open up interesting perspectives for the development of stable electronic devices.

Introduction

Bulk heterojunction organic solar cells (BHJ OSCs) have attracted a considerable interest as a promising technology for photovoltaic conversion owing to their light weight, mechanical flexibility and lower environmental impact.[1,2] In addition, power conversion efficiencies (PCE) higher than 18% have been recently reported for single-junction BHJ OSCs.[3-5] These photovoltaic performance result from the optimization of different parameters. The development of innovative multi-component (binary, ternary or quaternary) photoactive layers based on new conjugated donor polymers [6,7] and non-fullerene acceptor materials [8-10] has led to better complementary absorption properties and energy level alignment. The introduction of efficient electron and hole transport materials have also been shown to be critical to improving the transport of photogenerated charges and extracting them at the electrodes of OSCs,[11-16] while heterointerface engineering in OSCs, as well as in Perovskite solar cells,[17-19] is also decisive in increasing both their efficiency and stability. Processing optimization of OSCs plays a key role on the nanoscale morphology of the organic layers, and hence on the photovoltaic performance.[20,21]

The architecture of the devices can also impact the performance of OSCs. Inverted OSCs, which extract electrons from the transparent indium tin oxide (ITO) electrode by depositing an electron transport layer (ETL), have the advantage of using more stable top electrodes such as silver and hence the potential to exhibit both high efficiency and enhanced device lifetime over that of conventional architectures.[22-24]

Due to its high electron mobility (10^2 $cm^2/V.s$),[25] high transmission in the visible (90%),[26] wide band gap (3.2-3.4 eV) and high chemical stability,[27,28] zinc oxide (ZnO) remains the most studied material used as ETL in inverted OSCs.[29,30] In the case of P3HT:$PC_{61}BM$-based inverted OSCs, the bottom of the ZnO conduction band (*ca*. - 4.3 eV) is ideally located between the work function of ITO (*ca*. - 4.7 eV) and the LUMO level of the $PC_{61}BM$ acceptor (*ca*. - 3.9 eV).[31-33]

On the other hand, cerium oxide (CeO_2), one of the most abundant rare earth oxides on earth, has remarkable optical properties similar to those of ZnO, such as a wide bandgap of 3.2 eV[34] that can be modulated (3-3.6 eV),[35] a good transparency in the visible region, a high dielectric constant ε (24.5)[34] and a high refractive index (2.2-2.8).[36,37] It also exhibits high absorption in the ultraviolet region, [38] as well as high thermal (550°C) and chemical stability.[39-41] Thanks to the absence of the 4f electron in Ce^{4+}, CeO_2 has exceptional photoluminescent properties.[42] It

has been used in toxic gas detection,[43] UV filters,[44] medical diagnostics,[45] white light-emitting diodes [46] and electronics (capacitors,[47] RRAM resistive memories,[48] gate dielectric materials in CMOS devices [49] and fuel cells [50]). Although ZnO was long considered as a standard material for photocatalysis, cerium oxide is now the most widely used semiconductor for the destruction of organic pollutants under solar irradiation,[51,52] particularly for water treatment.[53]

In recent years, the doping of ZnO with other metal oxides such as cerium oxide CeO_x, has attracted considerable attention from researchers. CeO_2 can be reduced to its non-stoichiometric form CeO_{2-x} with a value of x varying between 0 and 0.5.[54,55] Mixed ZnO:CeO_x layers have been developed for gas sensors,[56] antibacterial applications [57] and UV filters.[58]

This type of mixed layer has recently been used as an ETL in perovskite-based hybrid solar cells. Doping of ZnO with CeO_x improves the stability of the ZnO/perovskite interface, reduces the work function of the ETL leading to a lowering the energy barrier between the ETL and the perovskite, hence resulting in more efficient photovoltaic devices.[59] ETL thin films based on pure CeO_x have also been shown to improve the photovoltaic efficiency and stability of perovskite hybrid cells.[60-65] Thus, since 2017, CeO_x has been used as an ETL in hybrid perovskite solar cells [59,66,67] and more recently as a transparent conductive layer based on cerium-doped ITO with a view to preparing tandem hybrid perovskite cells.[68]

To our knowledge, CeO_x has been used much less frequently as an ETL in OSCs. The work of Li *et al.*[33] in 2014 showed that the introduction of a nanostructured CeO_x layer, prior to the deposition of the aluminium top electrode in a direct architecture ITO/PEDOT:PSS/BHJ/CeO_x/Al, led to efficient light trapping to improve light absorption by the photoactive BHJ layer and thus photovoltaic performance; a conversion efficiency of 8.52% was achieved with PBDTBDD and $PC_{61}BM$, representing an increase of 48% compared with the device prepared with a planar aluminium layer without CeO_x. A second article dedicated to OCSs incorporating CeO_x as ETL was then published in 2015 and focused on P3HT:$PC_{61}BM$-based inverted cells, showing however very low photovoltaic performances (PCE < 0.7%).[69] In this case, the ETL layer was deposited from a colloidal solution of CeO_x nanoparticles prepared from cerium nitrate.

Given the good performance associated with CeO_x in the field of hybrid perovskite solar cells since 2017, we thought it would be interesting to reconsider the development of P3HT:$PC_{61}BM$-based inverted OSCs using a new formulation for the deposition of the CeO_x layer. In this work, the formation of the CeO_x layer has been optimized and characterized by different analytical

techniques such as X-ray diffraction (XRD) and X-ray photoelectron spectroscopy (XPS). Inverted OSCs based on P3HT:$PC_{61}BM$ as the photoactive layer[70] and ZnO as the electron transport layer, have been then prepared and used as reference devices. ZnO has been either replaced with or doped with CeO_x, and the corresponding solar cells have been tested and compared with ZnO-based reference devices.

Experimental

Preparation of CeO_x layers (ETL). The precursor solution of CeO_x was obtained by dissolving 196 mg of cerium (III) acetate hydrate $Ce(OAc)_3.yH_2O$ (99.9%, Aldrich) in 6 mL of isopropanol (99.9 %, Merck) and 2 mL of acetic acid. The transparent solution was stirred on a hot plate overnight at 45°C to give a white colloidal suspension. The introduction of acetic acid is known to accelerate the hydrolysis process.[33,71] The suspension (80 µL) was deposited by spin-coating on cleaned glass slides or ITO substrates under rotation at a speed of 2000 rpm for 60 s. Thermal annealing (TA) at different temperature was tested to generate the formation of CeO_x. Optimized conditions found for the fabrication of the best OSCs correspond to a thermal treatment at 200°C for 15 min.

Preparation of ZnO layers (Reference ETL). A sol-gel was obtained by mixing zinc (II) acetate dihydrate $Zn(OAc)_2.2H_2O$ (98%, Acros Organics) (196 mg) and ethanolamine (54 μL, 1 equiv.) in absolute ethanol (6 mL).[72] The mixture was stirred overnight at 45°C to produce a transparent solution. 80 µL of the latter were then deposited by spin coating on cleaned ITO or glass substrates rotating at a speed of 2000 rpm for 60 s. Finally, the prepared samples were annealed in an oven at 180°C for 15 min. The thickness of the ZnO layer measured by profilometry was 25 +/- 1 nm.

Preparation of ZnO layer doped with CeO_x as ETL. This mixed ZnO:CeO_x layer was prepared using the procedure reported by Meng *et al*.[59] from a solution of 193 mg of $Zn(OAc)_2.2H_2O$ in 2 mL of 2-methoxyethanol in the presence of 56 µL of ethanolamine and *ca*. 3 mol % of $Ce(OAc)_3.yH_2O$ (10 mg). *Note that the molar percentage of cerium acetate vs zinc acetate has been calculated on an anhydrous basis.* This solution was stirred overnight at room temperature before deposition (80 µL) by spin coating onto ITO substrates subjected to a rotational speed of 4000 rpm for 30 seconds. The resulting thin films were annealed at 200°C for one hour. During this study, cells with a pure ZnO layer were also prepared using the same procedure without the presence of cerium acetate.

Preparation of the photoactive P3HT-$PC_{61}BM$ layer. P3HT (74000 Daltons, 97.3% of regioregularity) and $PC_{61}BM$ (purity > 99%) were purchased from Ossila. The photoactive layer was prepared from a solution consisting of a 1:0.6 mass ratio of donor to acceptor in chloroform at a total concentration of 25 mg/mL. This mixture was stirred for 2 h at 35°C until the products were completely dissolved. Then, 80 µL of this mixture were deposited by spin coating on glass or on the ETL of the inverted OSCs. Deposition was carried out in air on the substrate under a rotation speed of 2000 rpm for 35 seconds. The resulting photoactive thin film was then annealed on a hot plate at 110°C for 3 minutes in a glove box under an inert atmosphere (Argon). The thickness of this layer on glass was 174 +/- 3 nm as determined by profilometry.

Inverted OSCs fabrication and characterization. Pre-patterned indium-tin oxide (ITO) coated glass slides of 24 × 25 × 1.1 mm with a sheet resistance of $R_s = 7\ \Omega\ sq^{-1}$ were purchased from Visiontek Systems. The ITO substrates were cleaned in ultrasonic baths for at least 15 minutes for each step in the following order: deionized water with detergent (Deconex® 12 PA-x solution, 2 drops), then acetone and finally ethanol. Once dried under a steam of air, a UV-ozone plasma treatment (Ossila UV/Ozone cleaner E511) was performed for 15 minutes ensuring elimination of residual organic contaminants of the ITO substrates which were used rapidly for the next step. As described above, a layer of ZnO, CeO_x or ZnO:CeO_x and a layer of P3HT:$PC_{61}BM$ were successively deposited in ambient atmosphere. After TA of the latter at 110°C for 3 minutes under inert atmosphere, the substrates were fixed to a holder before being covered with masks featuring discoidal patterns with a surface area of 0.28 cm^2 and transferred to a chamber under a vacuum of between 10^{-6} and 10^{-7} mbar. Finally, a layer of molybdenum oxide MoO_3 (6 nm), used as a hole transporter, and a layer of silver Ag (100 nm), used as top electrode, were successively deposited by thermal evaporation.

J-V curves of organic solar cells were recorded on devices within a glove-box using a Keithley 236 source-measure unit (Beaverton, USA) and a home-made acquisition program. The light source is an AM1.5 Solar Constant 575 PV simulator (Steuernagel Lichttechnik, equipped with a metal halogen lamp, 100 mW cm^{-2}, Morfelden-Walldorf, Germany). The light intensity was measured by a broad-band power meter (13PEM001, Melles Griot, Rochester, USA). No mask was used during the measurement of the J-V characteristics to define the active area of the cells. However, the architecture of the OSCs has been designed to neglect or minimize the impact of the edge effect and device layout on the PV performance. Thus, our cells exhibit a discoidal shape and a large surface area of 0.28 cm^2 which allow to neglect or limit the overestimation of the photovoltaic performance in agreement with results from the literature.[73] External quantum

efficiency (EQE) spectra were measured under an inert atmosphere with a QUESA–1200 (TFSC Instrument) using monochromatic wavelengths emitted by LEDs.

Results and discussion

Preparation of CeO_x and ZnO layers and their characterization

CeO_x layers have been already prepared in the literature from cerium (IV) isopropoxide,[33] cerium (III) nitrate[61] or cerium (III) acetylacetonate.[60,62,66] Inspired by the recent work of Meng *et al*. on the doping of ZnO with CeO_x in perovskite-type solar cells,[59] we have used cerium (III) acetate. A solution of the latter, dissolved in isopropanol in the presence of acetic acid, was stirred at 45°C overnight, producing a white colloidal suspension.

From this suspension, a solid sample obtained after solvent evaporation and vacuum drying, was analysed by thermogravimetric analysis (TGA) to determine the temperature at which cerium oxide was formed. The TGA curve showed that the transformation of the precursor powder into CeO_x started just after 200°C and was complete above 450°C (Figure 1).

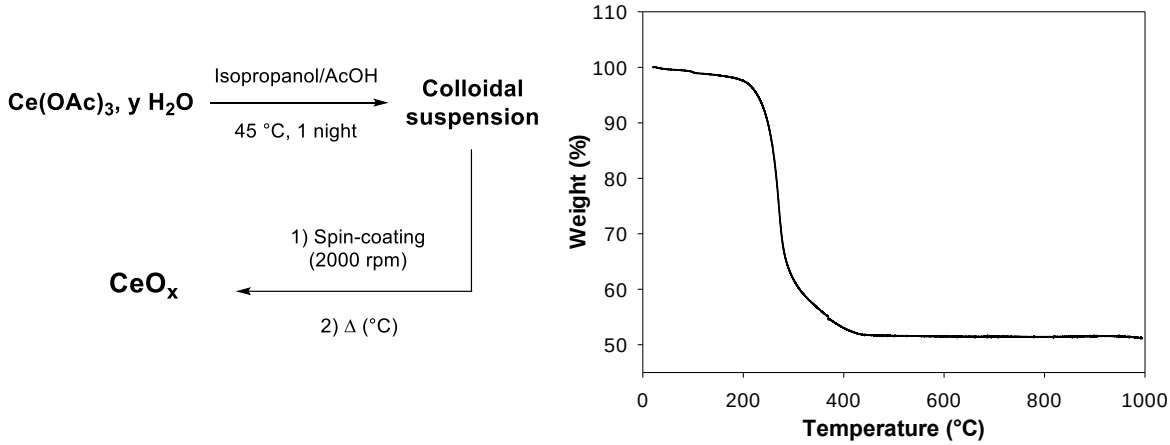

Figure 1. Synthesis of CeO_x and TGA curve of the CeO_x precursor solid (2.77 mg) recorded under nitrogen at 10°C/min.

XRD analysis was first carried out on a film deposited on glass by drop-casting the colloidal solution followed by thermal annealing (TA) at 450°C for 15 minutes. Figure 2 showed diffraction peaks located at 2θ values of 28.57°, 33.13°, 47.53°, 56.40° and 59.30° which could be assigned to the (111), (200), (220), (311) and (222) peaks of the CeO_2 structure[74,75] in agreement with the powder diffraction file of crystalline CeO_2 (PDF2 00-043-1102). This result

highlights the formation of crystalline CeO_2 when the film is annealed at 450°C. In contrast, the diffractogram of a drop cast or spin coated film treated at 200°C for 15 minutes shows the absence of peaks indicating the amorphous character of the film.

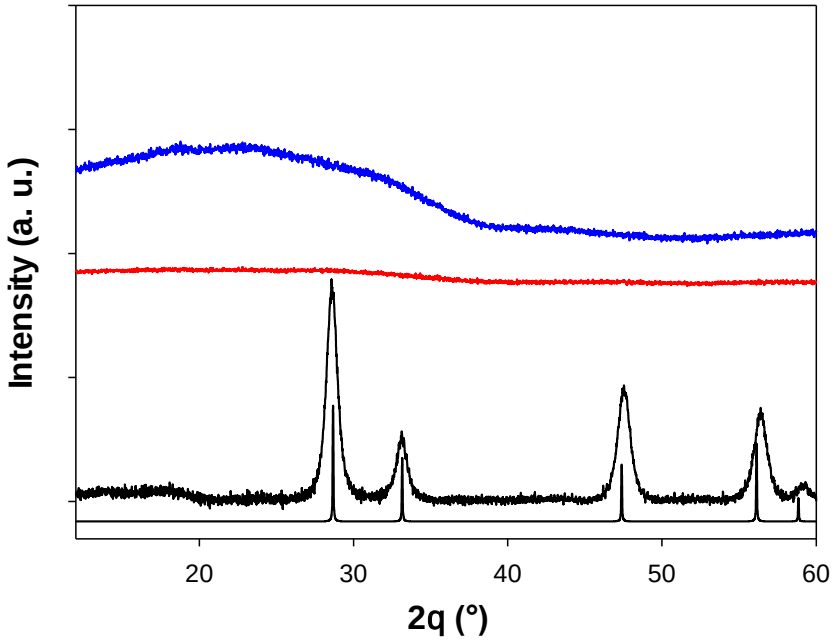

Figure 2. XRD diagrams of films obtained by deposition of the colloidal suspension on glass by i) drop casting followed by TA at 450°C/15 min (black curve, in the presence of the theoretical XRD peaks for CeO_2) or at 200°C/15 min (red curve) and ii) spin coating followed by TA at 200°C/15 min (blue curve).

XPS analyses were carried out to determine the chemical composition of the thin films. XPS spectra were recorded on a commercial cerium acetate powder $Ce(III)(OAc)_3.yH_2O$ and on three thin films on glass, the first without TA and the other two annealed at 200°C or 450°C for 15 minutes (Figure S1). The thin films were prepared by depositing the CeO_x precursor solution (80 µL) by spin coating on cleaned glass slides rotating at 2000 rpm for 60 s.

The Ce3d XPS core-level spectrum of the thin film without annealing showed the two 3d electron components of Ce^{3+}, $3d_{3/2}$ (901.9 eV) and $3d_{5/2}$ (883.3 eV), resulting from spin-orbit coupling (Figure 3b).[76,77] For each of these components, a significant shoulder was observed at lower energies at 897.9 eV and 879.3 eV, for $3d_{3/2}$ and $3d_{5/2}$ respectively, as shown by the deconvolution of the spectrum (Figure 3b). These shoulders, associated with blue peaks in the 3d electron region of the XPS spectrum, are characteristic of cerium and result from hybridization of its 4f electronic levels with the 2p orbitals of neighbouring oxygen atoms (Ce-

O).[78] Thus, for Ce^{3+}, each $3d_{3/2}$ and $3d_{5/2}$ component consists of two doublets at 901.9 eV/897.9 eV and 883.3 eV/879.3 eV, respectively. For each doublet, the two most intense peaks at the highest energy correspond to the $Ce3d^{9}4f^{1}O2p^{6}$ electronic structure, while the shoulders at the lowest energy correspond to the $Ce3d^{9}4f^{2}O2p^{5}$ electronic structure. As expected, without TA of the film, there was no trace of Ce^{4+} and therefore no formation of cerium dioxide CeO_2. In the case of cerium acetate, each $3d_{3/2}$ and $3d_{5/2}$ component consisted of two doublets at 902.1 eV/898.1 eV and 883.5 eV/879.5 eV, respectively (Figure 3a). The XPS spectra of the cerium acetate and that of the unheated thin film are very close for the part of the spectrum relating to the 3d electronic levels of cerium.

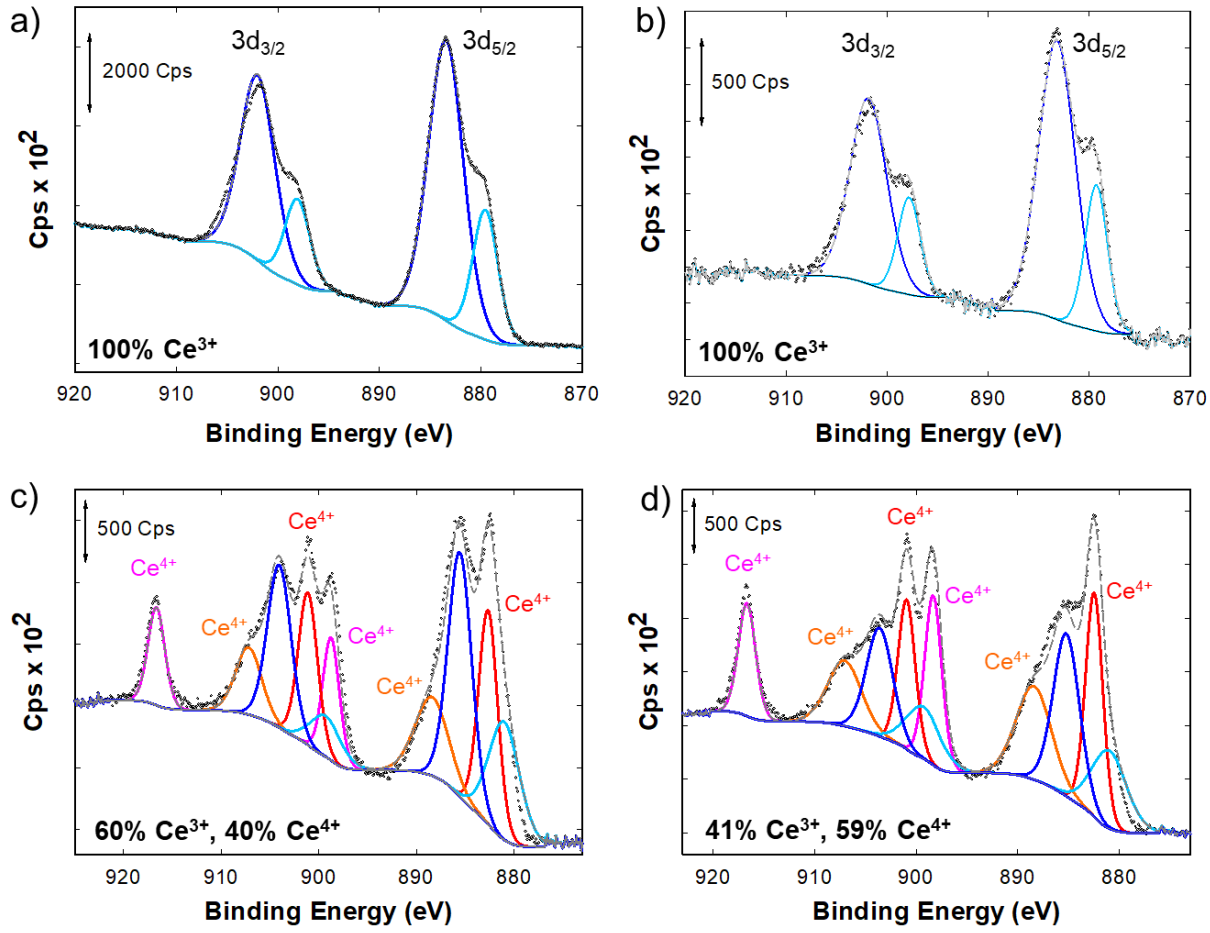

Figure 3. XPS core level spectra of cerium 3d electronic levels for cerium(III) acetate (a), thin films of the CeO_x precursor without TA (b), and after treatment at 200°C (c) or 450°C (d) for 15 min.

On the other hand, the carbon C1s XPS core-level spectrum of cerium(III) acetate showed an intense band centred at 288.3 eV corresponding to the carbon atoms of the -O-C=O type from the acetate groups whereas this band nearly disappeared for the thin film obtained directly after

deposition of the CeO_x precursor solution (Figure S2). As expected, this result clearly showed the efficiency of the hydrolysis of the acetate groups.

After treatment of the thin films at 200°C for 15 minutes, the XPS spectrum of the 3d electron region became more complex and new peaks characteristic of Ce^{4+} appeared in addition to those of Ce^{3+} described previously, confirming the partial formation of cerium dioxide CeO_2 (Figure 3c). Using deconvolution, two new systems could be observed, consisting of three peaks at 916.7 eV/907.2 eV/901.2 eV for the $3d_{3/2}$ component and 898.8 eV/888.5 eV/882.7 eV for the $3d_{5/2}$ component, peaks corresponding to the electronic structures $Ce3d^94f^0O2p^6$, $Ce3d^94f^1O2p^5$ and $Ce3d^94f^2O2p^4$, respectively. The isolated peak at 916.7 eV in the $3d_{3/2}$ component, unequivocally indicates the formation of Ce^{4+}. Thus, these XPS results clearly showed that TA at 200°C for 15 min was sufficient to form CeO_2. Deconvolution of the spectrum and integration of the peaks enabled us to estimate the percentage of Ce^{4+} formed at 40%, in agreement with a $CeO_{1.70}$ stoichiometry (x = 1.70). This stoichiometry is relatively close to those obtained for CeO_x layers used to produce organic solar cells (x = 1.72).[33] Finally, TA at 450°C for 15 min increased the proportion of Ce^{4+} from 40% to 59%, leading to a $CeO_{1.79}$ (x = 1.79) stoichiometry (Figure 3d).

Finally, oxygen O1s XPS core-level spectra of thin films thermally annealed at 200°C and 450°C are displayed in Figure S3, showing a main band at 532.2 eV with a shoulder at lower energy indicating the presence of at least two types of oxygen species. This main band is due to the presence of hydroxyl OH groups and adsorbed water or O_2 molecules on the surface. After deconvolution of the XPS spectra of thin films thermally annealed at 200°C and 450°C, the less intense bands at 530.3 eV and 530.1 eV, associated to the shoulder, are characteristic of oxygen species O^{2-} bound to Ce^{3+} or Ce^{4+}.[74] The small difference of energy for these two bands results from the binding energy difference of 0.3 eV between oxygen bound to Ce^{3+} and Ce^{4+}. Comparing the surface area of the latter band (O1s-Ce) with the whole signals of Ce 3d, allowed us to estimate the relative O/Ce ratio for the thin films thermally annealed at 200°C (O/Ce = 2.03) and 450°C (O/Ce = 2.40). As expected, the O/Ce ratio was higher for thin films annealed at 450°C. However, these ratios were higher than expected and differed from the O/Ce values, 1.70 and 1.79 respectively, obtained from the integration of the 3d signals characteristic of Ce^{3+} and Ce^{4+}. This difference could be due to the lack of accuracy in deconvoluting the O1s XPS spectra because of the presence of the intense band attributed to OH and H_2O/O_2 pollution.

In summary, the XPS analyses demonstrated that it was possible to partially generate cerium dioxide CeO_2 after treatment of a thin film at 200°C for 15 min, this process leading to the

formation of amorphous CeO_2, in agreement with the absence of diffraction peaks noted during the XRD analysis. Indeed, amorphous CeO_2-based heterostructures have already been described in the literature for the electrochemical reduction of CO_2,[79] the catalysis of propane dehydrogenation[80] or the electroreduction of CO_2 into HCOOR formate.[81] It is therefore conceivable to use these CeO_x thin films produced at a relatively low temperature for applications in organic electronics.

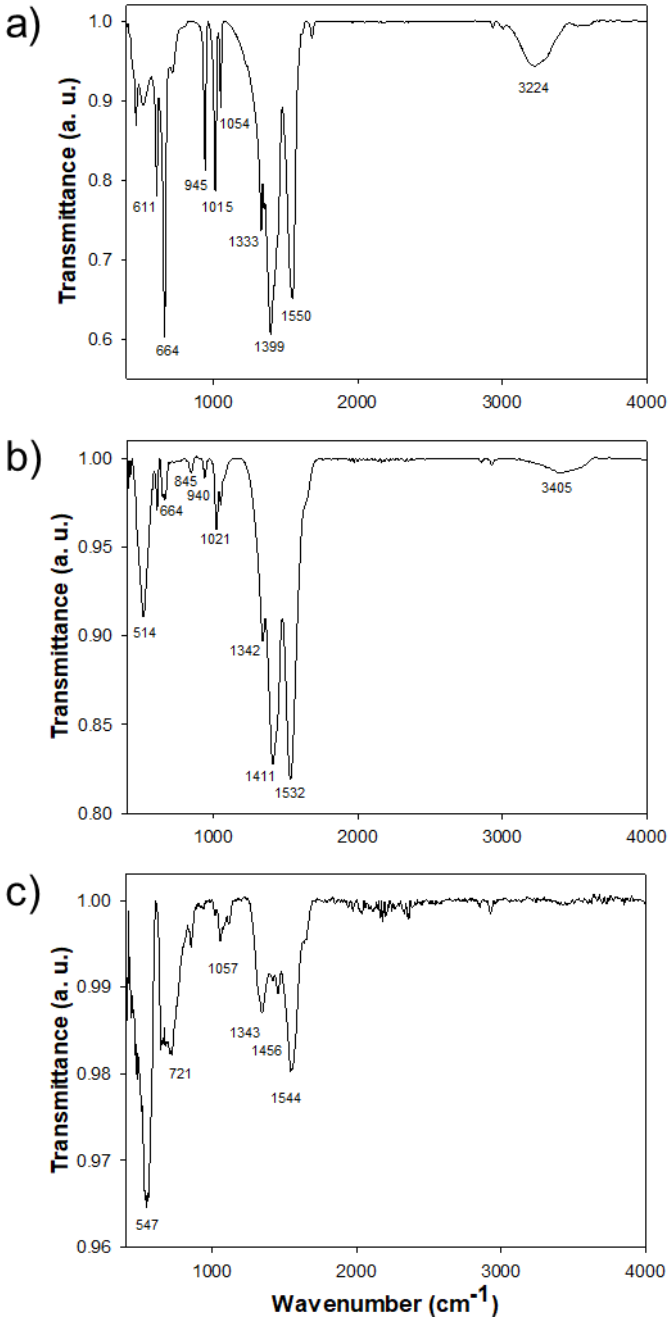

Figure 4. Attenuated total reflection mode FT-IR spectra of cerium acetate $Ce(OAc)_3.yH_2O$ (a) and CeO_x thin films annealed at 200°C (b) and 450°C (c) for 15 min.

CeO_x thin films on glass, obtained after annealing at 200°C or 450°C for 15 minutes, and commercial cerium acetate hydrate ($Ce(OAc)_3.yH_2O$) powder were also studied by Fourier transform infrared spectroscopy (FT-IR) in attenuated total reflection mode. The FT-IR spectra recorded between 400 and 4000 cm^{-1} are shown in Figure 4. For hydrated cerium acetate powder, the broad band centred at 3224 cm^{-1} was associated with the O-H stretching mode (presence of water). Based on infrared spectroscopy data for sodium acetate in the solid state,[82] the peaks at 1550 cm^{-1} and 1399 cm^{-1} could be attributed to the antisymmetric and symmetric stretching vibrations of the C-O group (ν_{C-O}) of the acetate group respectively, while the peak at 664 cm^{-1} corresponded to deformation (δ_{C-O}).

Assuming that the IR spectra of a powder and of a thin film on glass could be compared, the film treated at 200°C showed a significant decrease in the peak at 664 cm^{-1} (δ_{C-O}) as well as that of the band linked to the O-H stretching frequency present in cerium acetate. This result suggested the partial transformation of cerium acetate. The three peaks at 1342 cm^{-1}, 1411 cm^{-1} and 1532 cm^{-1} could result from different contributions, both from the remaining cerium acetate and from new signals corresponding to the formation of cerium oxide. In the case of the thin film annealed at 450°C, there was a significant decrease in the bands in the 1300-1700 cm^{-1} region suggesting greater conversion to CeO_2, the peaks present could be related to the formation of carbonate species formed by coordination of CO_2 on the CeO_2 surface.[83] In addition, broad and intense signals between 500 cm^{-1} and 750 cm^{-1}, already present in the thin film annealed at 200°C, were characteristic of Ce-O stretching vibrations according to the literature,[83] confirming the formation of cerium oxide. These results agree with the measurements made by XPS spectroscopy.

The transmittance and wettability of ZnO and CeO_x thin films were evaluated by UV-visible spectroscopy and contact angle measurements, respectively. CeO_x thin films were prepared by spin-coating the CeO_x precursor solution followed by TA at 200°C for 15 minutes. As shown in Figure S4, both oxides show good transparency in the visible range, with an optical transmission of over 95% between 400 and 1000 nm. However, the CeO_x thin film exhibited a better transmission at 300 nm than the ZnO film. The bandgap energy values E_g were determined using the Tauc method affording values of 3.50 and 3.55 eV for ZnO and CeO_x, respectively. The value of E_g for CeO_x was consistent with a value of x lower than 2 and therefore the presence of Ce^{3+} ion.[34,66] Contact angles measured on a drop of water deposited on the ZnO and CeO_x layers were 46° and 51°, respectively (Figure S5), indicating that these

two layers exhibited similar surface properties, although the CeO_x layer was slightly more hydrophobic.

P3HT:$PC_{61}BM$ inverted OSCs with ZnO or CeO_x as ETL

The reference photoactive layer composed of poly(3-hexylthiophene) (P3HT) and methyl [6,6]-phenyl-C_{61}-butanoate ($PC_{61}BM$) was chosen for the evaluation of CeO_x as ETL in inverted OSCs.[84,70] It was prepared by spin-coating a solution consisting of a 1:0.6 mass ratio of P3HT and $PC_{61}BM$ in chloroform at a total concentration of 25 mg/mL. The optical spectrum of a thin-film spin-coated on glass showed a broad absorption band with a maximum at 493 nm associated to the absorption of P3HT (Figure S6). After TA at 110°C for 3 minutes, a bathochromic shift of the absorption maxima by 23 nm and an increase in the intensity of the absorption band together with the appearance of a shoulder at 597 nm were observed, leading to an improvement in the absorption of the active layer in the visible range. The bandgap of P3HT was estimated from the edge of the main band at lower energy leading to a value of 1.90 eV (Figure S6). As expected, these results showed that TA led to a reorganization of the film, resulting in stronger intermolecular π-π interactions and an increase in the crystallinity of P3HT.[21,85,86] Accordingly, AFM analysis of the P3HT:$PC_{61}BM$ active layer showed that TA increased the surface roughness of the photoactive layer from 0.76 nm to 2.86 nm. This observation together with the appearance of a more structured surface for the annealed layer agrees with the higher crystallinity of the material (Figure S7).

Photoelectron spectroscopy in air (PESA) measurements were carried out on thin films of P3HT and $PC_{61}BM$ (Figure S8). The energy of their HOMO levels has been determined at the threshold of current detection of a logarithmic representation (Figure 5) and after a subsequent fitting procedure described in Supporting Information. This method which differs significantly from the widely used tangent method applied in the high energy region of the PESA spectrum, allows for a more accurate determination of the HOMO level which is related to the minimal energy required for the extraction of electrons from the considered material upon UV excitation. A value of - 4.70 eV was measured for P3HT which is in good agreement with that measured by Baran and co-workers in their review (- 4.55 eV).[87] The LUMO level of P3HT was then calculated at - 2.80 eV by considering its optical band gap. On the other hand, the energy of the HOMO level of $PC_{61}BM$ was determined at - 6.05 eV while the energy of its LUMO level (- 3.90 eV) was taken from the literature.[33]

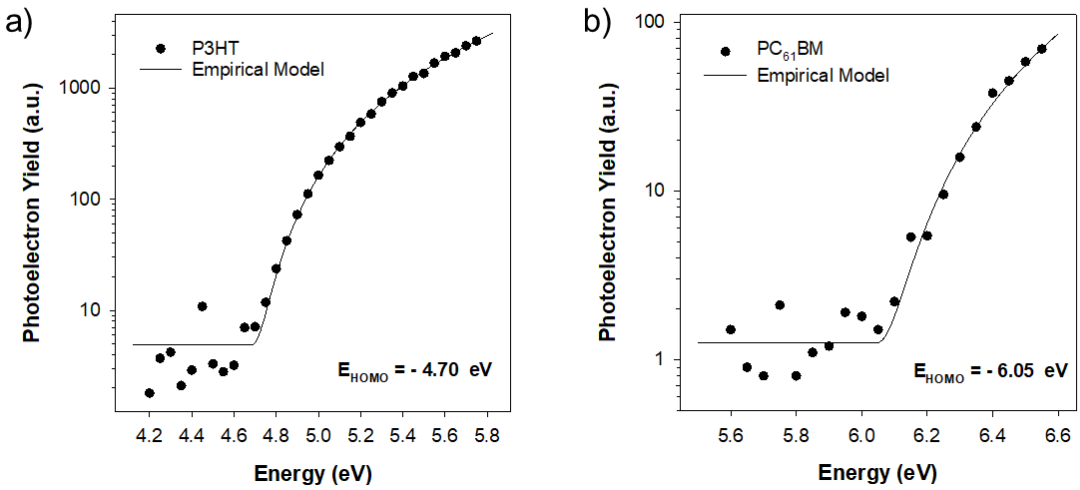

Figure 5. Logarithmic representations of PESA spectra together with the fitted curves obtained for P3HT (a) and $PC_{61}BM$ (b) using an empirical model to determine the HOMO levels.

To assess the potential of CeO_x as an ETL in inverted OSCs, we first fabricated and characterized reference devices based on ITO/ZnO/P3HT:$PC_{61}BM$/MoO_3/Ag and then replaced ZnO with CeO_x. The energy levels of the materials involved in the devices are displayed in Figure 6. The valence band maximum measured by ultraviolet photoelectron spectroscopy (UPS) at - 7.50 eV was taken from literature for ZnO[88] and CeO_x,[66] respectively. Considering the observed optical band gap E_g, the conduction band energy minimum was determined to be - 4.00 eV and - 3.95 eV, respectively. Thus, CeO_x exhibited a suitable energy level which was expected to facilitate the electron extraction from the P3HT-$PC_{61}BM$ photoactive layer to the ETL.

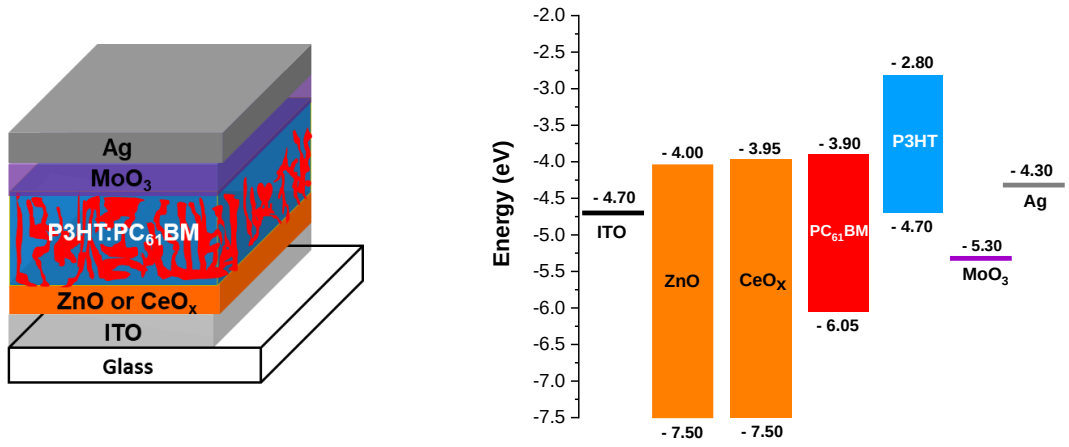

Figure 6. Inverted BHJ OSC architectures and corresponding energy diagram.

Figure 7a shows the J-V current-voltage density characteristics of the cells based on ZnO before and after TA of the P3HT:$PC_{61}BM$ active layer. The photovoltaic parameters extracted from the J-V curves are summarized in Table 1. The best results were obtained after TA, leading to a PCE conversion efficiency of 3.21%, associated with an increase in the short-circuit current density J_{sc} and the fill factor FF, which rose from 4.08 to 9.20 mA cm^{-2} and from 31 to 60% respectively. This result could be explained by improvements in: i) the absorption properties of the active layer, ii) the interfaces between the active layer and the electrodes (lower series resistance R_s and higher shunt resistance R_{sh}) and iii) the morphology of the active layer. In addition, an average PCE value of 3.09% was obtained for a series of 11 cells produced under the same conditions, indicating a good reproducibility. These performances are those expected for the P3HT:$PC_{61}BM$ pair, which validates our experimental conditions.[72]

Table 1. Photovoltaic parameters of the best ITO/ZnO/P3HT:$PC_{61}BM$/MoO_3/Ag cell before and after TA at 110°C for 3 min.

Conditions	J_{sc} (mA cm^{-2})	V_{oc} (V)	FF (%)	PCE (%)	R_s (Ω cm^2)	R_{sh} (Ω cm^2)	PCE_{av} (%)	Number of cells
w/o TA	4.08	0.66	31	0.85	99	258	0.80	4
TA	9.20	0.57	60	3.21	9	735	3.09	11

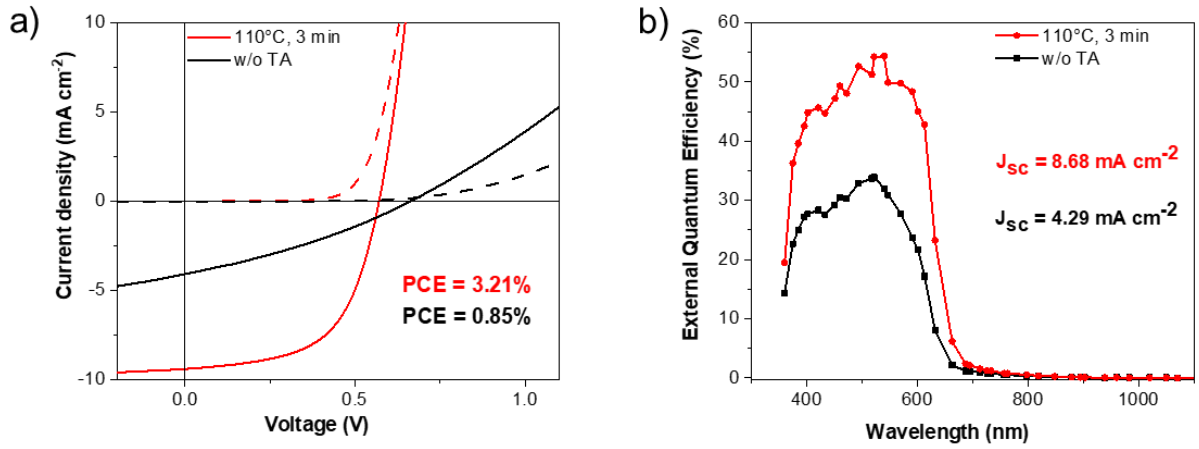

Figure 7. a) J-V characteristics of the best ITO/ZnO/P3HT:$PC_{61}BM$/MoO_3/Ag cell under illumination (solid line) and in the dark (dashed line) with and without TA of the photoactive layer. b) EQE spectra of the best ITO/ZnO/P3HT:$PC_{61}BM$/MoO_3/Ag cell before and after TA.

The external quantum efficiency (EQE) spectrum of the device whose photoactive layer has undergone TA showed a broad band centred at 540 nm with a maximum of 54% and a J_{sc} value of 8.68 mA cm^{-2} calculated by integrating the area under the curve. On the other hand, the photoresponse of the device that had not undergone TA was less intense, with a maximum EQE

value of 34% at 522 nm and a calculated J_{sc} value of 4.29 mA cm^{-2} (Figure 7b). These J_{sc} values calculated from the EQE spectra agreed with those obtained from the J-V curves under illumination.

ZnO was then replaced with CeO_x to evaluate its potential as ETL in inverted BHJ OSC with the following architecture ITO/CeO_x/P3HT:$PC_{61}BM$/MoO_3/Ag (Figure 6). CeO_x layers were prepared by depositing the precursor solution (80 µL) onto ITO substrates rotating at 2000 rpm. The resulting layers were then subjected to a TA by varying the annealing temperature and time. The inorganic layers were annealed at 150°C, 200°C, 300°C or 450°C for 15 minutes. The J-V characteristics of the cells under illumination at 100 mW cm^{-2} are shown in Figure 8a and all the parameters are listed in Table 2. A photovoltaic effect with a PCE of 0.88% was observed when the ETL was annealed at 150°C. Devices with an ITO/P3HT:$PC_{61}BM$/MoO_3/Ag structure, in which the P3HT:$PC_{61}BM$ active layer was directly deposited on the ITO substrate, showed no photovoltaic effect. These results evidenced the interest of the CeO_x layer for electron transport in inverted OSCs. In addition, an annealing at 200°C significantly improved cell performance, with a PCE reaching 1.71% (1.63% on average over 4 cells) associated with a current density J_{sc} of 8.60 mA cm^{-2}, a voltage V_{oc} of 0.45 V and a fill factor FF of 44% (R_s = 10 Ω cm^2, R_{sh} = 300 Ω cm^2). On the other hand, a TA above 200°C led to performance drops down to a PCE value of 0.35% after annealing at 450°C.

In a second step, the TA time was increased to 30 minutes. Figure 8b and the data in Table 2 showed that the photovoltaic conversion efficiencies were weakly affected. However, the annealing at 200°C for 30 minutes resulted in a decrease of the PCE value.

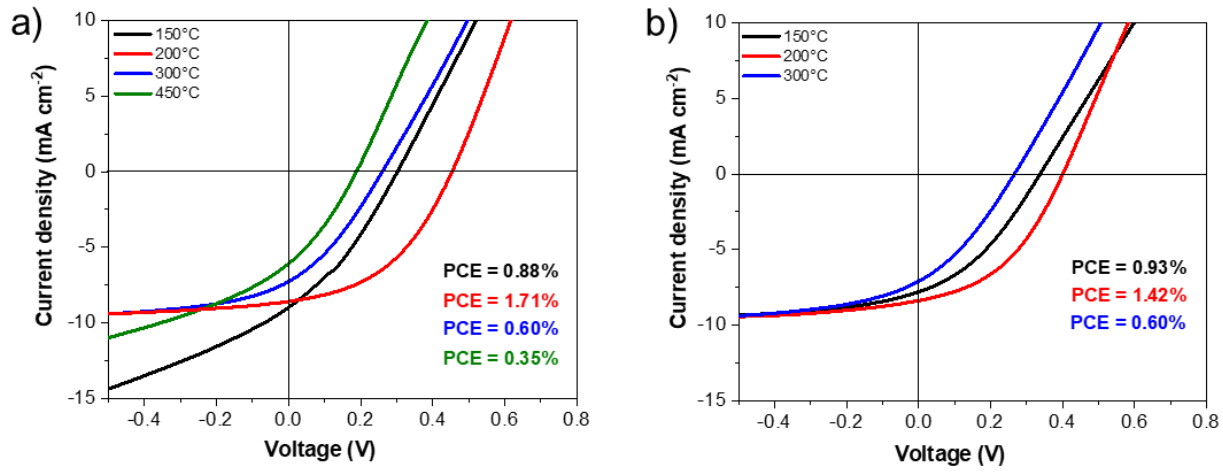

Figure 8. J-V characteristics of ITO/CeO_x/P3HT:$PC_{61}BM$/MoO_3/Ag devices under illumination at 100 mW cm^{-2} after annealing the CeO_x layer at different temperatures for 15 min (a) or 30 min (b).

Table 2. Photovoltaic parameters of ITO/CeO_x/P3HT:$PC_{61}BM$/MoO_3/Ag cells as a function of temperature and annealing time of the CeO_x layer.

TA	J_{sc} (mA cm^{-2})	V_{oc} (V)	FF (%)	PCE (%)	R_s (Ω cm^2)	R_{sh} (Ω cm^2)	$PCE_{av.}$ (%)	Number of cells
150 °C, 15 min	8.98	0.30	33	0.88	23	58	0.80	3
200 °C, 15 min	8.60	0.45	44	1.71	10	300	1.63	4
300 °C, 15 min	7.27	0.26	32	0.60	25	82	0.53	2
450 °C, 15 min	6.08	0.18	31	0.35	21	52	0.35	2
150 °C, 30 min	7.79	0.34	35	0.93	26	120	0.90	2
200 °C, 30 min	8.37	0.40	42	1.42	20	219	1.36	2
300 °C, 30 min	7.10	0.26	32	0.60	26	77	0.60	2

This work on optimizing the TA of the CeO_x layer showed that treatment at 200°C for 15 minutes led to the best photovoltaic performance. It appeared that the annealing temperature of 450°C, which produces a pure CeO_2 ceria phase, as shown by the X-ray powder diffraction pattern (Figure 2), led to a very low photovoltaic efficiency value (PCE = 0.35%). This result suggested that a crystalline character for the CeO_x layer is not conducive to the proper functioning of inverted OSCs. On the contrary, annealing at a lower temperature of 200°C led to more efficient cells that could achieve a PCE value of 1.71%.

To better understand this result, AFM analysis of ITO substrates coated with CeO_x films, annealed for 15 minutes at 200°C or 450°C, was carried out giving information on the effect of annealing on the layer morphology. AFM images (20 μm × 20 μm) showed no major change in the surface morphology of the films as a function of the TA temperature. In addition, the roughness of the films annealed at 200°C and 450°C were close at 3.7 nm and 3.2 nm, respectively (Figure S9). However, observation by AFM at larger scales (100 μm × 100 μm or 50 μm × 50 μm) showed that thin films annealed at 200°C led to a more homogeneous surface, whereas the ones annealed at 450°C exhibited isolated large crystalline clusters (Figures S9 and 9) likely associated with the growth of CeO_2 crystals, in agreement with XRD results. Figure 9 (5 μm × 5 μm) shows the growth of crystals with the presence of grain boundaries. The height of these crystalline clusters could reach 635 nm (Figure S10), a value much higher than the thickness of the P3HT:$PC_{61}BM$ active layer (173 nm). This result suggested that short circuits

could form in the device between the two electrodes. They also confirmed the low photovoltaic efficiency obtained with CeO_x films annealed at 450°C.

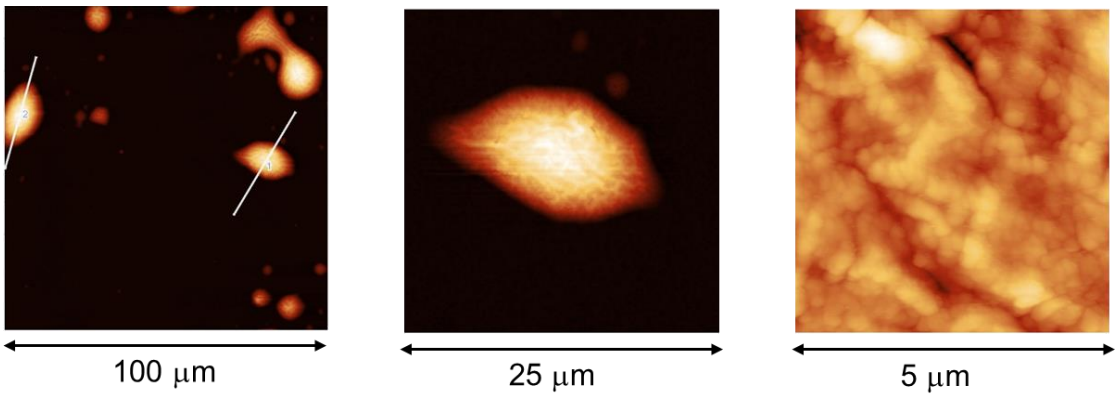

Figure 9. AFM images of different resolutions in size of the CeO_x layer annealed at 450°C for 15 min showing crystalline clusters.

The stability of the best devices with a ZnO or CeO_x layer was also tested during one month's storage in a glove box under 2.5 mbar of argon in ambient light at 20°C in the absence of organic solvents, with the amount of water and oxygen being less than 0.1 ppm for both (Tables S1 and S2). Interestingly, the photovoltaic efficiency of both ZnO- and CeO_x-based cells slightly increases reaching 110% and 125% of its initial PCE values after a storage period of 168 h and 384 h, respectively (Figure S11). For example, a maximum PCE value of 2.12% was obtained for CeO_x-based OSCs as compared to the initial PCE value of 1.71%. These variations can be explained in terms of ultraviolet (UV) activation of metal oxides, during storage in ambient light or J-V characteristic measurements under illumination. Indeed, UV light is often needed to activate inverted OSCs with ZnO as ETL for enhanced efficiency leading to increased conductivity and electron mobility.[89,90] In addition, after one month of storage, the PCE values for both types of cells were still higher than the initial ones, highlighting their good stability over time.

P3HT:$PC_{61}BM$ inverted OSCs using a mixed ZnO:CeO_x layer as ETL

In order to benefit from the positive impact of CeO_x on the stability of the devices while maintaining the photovoltaic performance obtained with ZnO, we attempted to dope the ZnO layer with a small amount of CeO_x. This approach was inspired by the recent results from Meng *et al*. who showed that doping ZnO with 3 mol % of CeO_x, as an ETL, improved the photovoltaic efficiency of perovskite-based hybrid cells (PCE > 19.5%) as well as their thermal

and UV stability.[59] The authors indicated that the addition of CeO_x stabilized the interface between the electron transport layer and the perovskite material, by creating an upward shift in the ZnO conduction band from - 4.43 eV (pure ZnO) to - 4.06 eV (ZnO with 3 mol % of CeO_x), facilitating electron transport to the electrode and reducing charge recombination at the interface.

Thus, P3HT:$PC_{61}BM$-based OSCs were prepared using a mixed ZnO:CeO_x layer as ETL (see Experimental Section). For comparison, cells with a pure ZnO layer were also prepared using the procedure described by Meng *et al*,[59] which slightly differed from our aforementioned procedure. The J-V characteristics of the cells under illumination at 100 mW cm^{-2} are shown in Figure 10 and the photovoltaic parameters extracted from the J-V curves are summarized in Table 3.

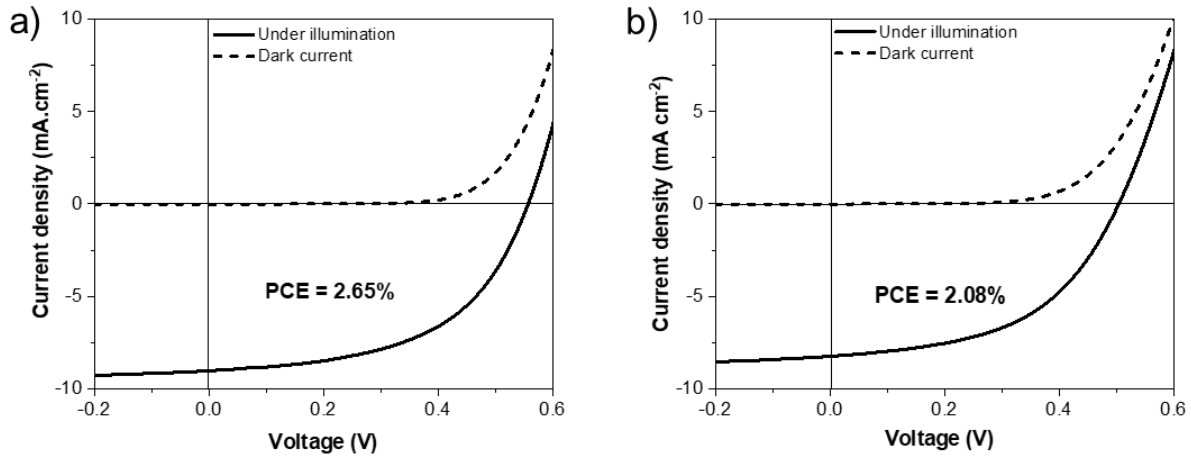

Figure 10. J-V characteristics of the best ITO/ZnO/P3HT:$PC_{61}BM$/MoO_3/Ag (a) and ITO/ZnO:CeO_x/P3HT:$PC_{61}BM$/MoO_3/Ag (b) cells under illumination and in the dark.

Table 3. Photovoltaic parameters of ITO/ETL/P3HT:$PC_{61}BM$/MoO_3/Ag cells.

ETL	J_{sc} (mA cm^{-2})	V_{oc} (V)	FF (%)	PCE (%)	R_s (Ω cm^2)	R_{sh} (Ω cm^2)	$PCE_{av.}$ (%)	Number of cells
ZnO	9.03	0.56	53	2.65	12	578	2.54	4
ZnO/CeO_x	8.25	0.50	50	2.08	15	476	1.90	4

Cells with a pure ZnO layer achieved a maximum photovoltaic efficiency of 2.65% (2.54% on average over 4 cells) associated with a current density J_{sc} of 9.03 mA cm^{-2}, a voltage V_{oc} of 0.56 V and a fill factor FF of 53%. In our case, contrary to literature results for perovskite-based devices,[59] the introduction of 3 mol % of CeO_x in the ZnO layer led to a decrease in photovoltaic

performance of inverted OSCs. Indeed, the best ZnO:CeO_x-based cell produced a slightly lower conversion efficiency of 2.08% (1.90% on average over 4 cells) associated with a J_{sc} value of 8.25 mA cm^{-2}, a V_{oc} voltage of 0.50 V and a fill factor of 50%.

The stability of the devices was also tested after one- and five-months' storage in a glove box in the same conditions as described above (Tables S3 and S4). It was interesting to note that the PCE of the best cell based on ZnO:CeO_x decreased very slowly to 2.03% after one month and then 1.77% after five months, hence retaining 97% and 85% of its initial PCE, respectively. In the case of the cell based on pure ZnO, the PCE value fell from 2.65% to 2.49% (93%) after one month and then to 2.01% (76%) after five months. Accordingly, the decrease in photovoltaic efficiency was slightly slower for ZnO:CeO_x-based devices than for pure ZnO-based cells. As described in Perovskite solar cells,[59] this result showed that the introduction of CeO_x helped improving the stability of the devices over time. This behaviour could be related to the higher chemical stability of CeO_x over ZnO,[66] the long-term stability of CeO_x under UV irradiation or the presence of 4f electrons in CeO_x limiting the UV-photodegradation of the organic photoactive layer of the OSCs.[59]

Conclusions

Solution-processed CeO_x layers were successfully prepared by spin coating on ITO substrates followed by a thermal annealing which was optimized. The formation of CeO_x was monitored and confirmed by TGA, XRD and FT-IR and XPS spectroscopy. These analytical techniques showed that a thermal annealing at moderate temperatures such as 200°C for 15 min was sufficient to form Ce^{4+} ions leading to an amorphous CeO_x layer, with a value of x reaching 1.70. Under these conditions, P3HT:PC_{61}BM inverted OSCs based on CeO_x achieved a photovoltaic efficiency of *ca*. 1.7%, as compared to the parent ZnO-based devices showing a maximum efficiency of *ca*. 3.2%. The analysis of the photovoltaic performances of the two types of devices over time showed an increase in PCE which can reach 125% after two weeks of storage in the case of CeO_x-based devices, however their stability over one month is close.

ZnO layers doped with 3 mol % of CeO_x were also used as ETL layers. Although the presence of few amounts of CeO_x induced a slight decrease of photovoltaic performance, a gain in stability was observed. Thus, this work showed that CeO_x could be effectively used as an ETL layer in inverted OSCs, potentially offering better stability than that achieved with ZnO. This preliminary work on the use of CeO_x as ETL could be extended to inverted BHJ OSCs with

new photoactive layers such as PM6-Y6 and, more generally, to other organic electronic devices.

Acknowledgements

The University of Tunis el Manar is thanked for the funding of the PhD thesis of S. A. carried out in collaboration with the University of Angers. S. A. was partly supported by the EUR LUMOMAT project and the Investments for the Future program (ANR-18-EURE-0012).

Bibliographic references

1. J. Chen, Y. Chen, L.-W. Feng, C. Gu, G. Li, N. Su, G. Wang, S. M. Swick, W. Huang, X. Guo, A. Facchetti and T. J. Marks, *EnergyChem*, 2020, **2**, 100042.
2. G. Zhang, F. R. Lin, F. Qi, T. Heumüller, A. Distler, H.-J. Egelhaaf, N. Li, P. C. Y. Chow, C. J. Brabec, A. K. Y. Jen and H.-L. Yip, *Chem. Rev.*, 2022, **122**, 14180-14274.
3. Q. Liu, Y. Jiang, K. Jin, J. Qin, J. Xu, W. Li, J. Xiong, J. Liu, Z. Xiao, K. Sun, S. Yang, X. Zhang and L. Ding, *Sci. Bull.*, 2020, **65**, 272-275.
4. Y. Cui, Y. Xu, H. Yao, P. Bi, L. Hong, J. Zhang, Y. Zu, T. Zhang, J. Qin, J. Ren, Z. Chen, C. He, X. Hao, Z. Wei and J. Hou, *Adv. Mater.*, 2021, **33**, 2102420.
5. K. Chong, X. Xu, H. Meng, J. Xue, L. Yu, W. Ma and Q. Peng, *Adv. Mater.*, 2022, **34**, 2109516.
6. L. Lu, T. Zheng, Q. Wu, A. M. Schneider, D. Zhao and L. Yu, *Chem. Rev.*, 2015, **115**, 12666-12731.
7. H. Fu, Z. Wang and Y. Sun, *Angew. Chem. Int. Ed.*, 2019, **58**, 4442-4453.
8. J. Yuan, Y. Zhang, L. Zhou, G. Zhang, H.-L. Yip, T.-K. Lau, X. Lu, C. Zhu, H. Peng, P. A. Johnson, M. Leclerc, Y. Cao, J. Ulanski, Y. Li and Y. Zou, *Joule*, 2019, **3**, 1140-1151.
9. W. Liu, X. Xu, J. Yuan, M. Leclerc, Y. Zou and Y. Li, *ACS Energy Lett.*, 2021, **6**, 598-608.
10. D. Luo, W. Jang, D. D. Babu, M. S. Kim, D. H. Wang and A. K. K. Kyaw, *J. Mater. Chem. A*, 2022, **10**, 3255-3295.
11. T. Yang, M. Wang, C. Duan, X. Hu, L. Huang, J. Peng, F. Huang and X. Gong, *Energy Environ. Sci.*, 2012, **5**, 8208-8214.
12. S. Rafique, S. M. Abdullah, K. Sulaiman and M. Iwamoto, *Renew. Sustain. Energy Rev.*, 2018, **84**, 43-53.
13. Z. Yin, J. Wei and Q. Zheng, *Adv. Sci.*, 2016, **3**, 1500362.
14. D. C. T. Nguyen, V.-D. Mai, V.-H. Tran, V.-P. Vu and S.-H. Lee, *Org. Electron.*, 2022, **100**, 106388.
15. A. Gusain, R. M. Faria and P. B. Miranda, *Front. Chem.*, 2019, **7**.
16. R. Alkarsifi, J. Ackermann and O. Margeat, *J. Met. Mater. Miner.*, 2022, **32**, 1-22.
17. P. Xu, J. Liu, J. Huang, F. Yu, C.-H. Li and Y.-X. Zheng, *New J. Chem.*, 2021, **45**, 13168-13174.
18. N. Nishimura, S. Mathew and T. N. Murakami, *New J. Chem.*, 2023, **47**, 4197-4201.
19. Z. Zhao, M. Zhai, C. Chen, H. Wang and M. Cheng, *New J. Chem.*, 2024, **48**, 11387-11393.
20. Y. Huang, E. J. Kramer, A. J. Heeger and G. C. Bazan, *Chem. Rev.*, 2014, **114**, 7006-7043.
21. M. T. Dang, L. Hirsch, G. Wantz and J. D. Wuest, *Chem. Rev.*, 2013, **113**, 3734-3765.
22. M. T. Lloyd, D. C. Olson, P. Lu, E. Fang, D. L. Moore, M. S. White, M. O. Reese, D. S. Ginley and J. W. P. Hsu, *J. Mater. Chem.*, 2009, **19**, 7638-7642.
23. P. Cheng and X. Zhan, *Chem. Soc. Rev.*, 2016, **45**, 2544-2582.

24. Q. Huang, J. Jing, K. Zhang, Y. Chen, A. Song, Z. Liu and F. Huang, *J. Mater. Chem. A*, 2022, **10**, 23973-23981.
25. K. Tian, B. Tudu and A. Tiwari, *Vacuum*, 2017, **146**, 483-491.
26. D. Gaspar, L. Pereira, K. Gehrke, B. Galler, E. Fortunato and R. Martins, *Sol. Energy Mater. Sol. Cells*, 2017, **163**, 255-262.
27. S. H. Sabeeh and R. H. Jassam, *Results Phys.*, 2018, **10**, 212-216.
28. X. D. Li, T. P. Chen, P. Liu, Y. Liu and K. C. Leong, *Opt. Express*, 2013, **21**, 14131-14138.
29. Z. Liu, R. Hu, J. Yu, R. Wang, J. Cheng, M.-m. Huo, T. Wu and L. Li, *Synth. Met.*, 2021, **274**, 116737.
30. S. Yang and H. Yu, *Chem. Eng. J.*, 2023, **452**, 139658.
31. N. Chander, S. Singh and S. S. K. Iyer, *Sol. Energy Mater. Sol. Cells*, 2017, **161**, 407-415.
32. S. Chen, J. R. Manders, S.-W. Tsang and F. So, *J. Mater. Chem.*, 2012, **22**, 24202-24212.
33. Z. a. Tan, L. Li, C. Li, L. Yan, F. Wang, J. Xu, L. Yu, B. Song, J. Hou and Y. Li, *Adv. Mater. Interfaces*, 2014, **1**, 1400197.
34. S. A. Ansari, M. M. Khan, M. O. Ansari, S. Kalathil, J. Lee and M. H. Cho, *RSC Adv.*, 2014, **4**, 16782-16791.
35. N. Pradhani, P. K. Mahapatra and R. N. P. Choudhary, *JPhys. Materials*, 2018, **1**, 015007.
36. F.-C. Chiu and C.-M. Lai, *J. Phys. D: Appl. Phys.*, 2010, **43**, 075104.
37. M. Balestrieri, S. Colis, M. Gallart, G. Schmerber, M. Ziegler, P. Gilliot and A. Dinia, *J. Mater. Chem. C*, 2015, **3**, 7014-7021.
38. R. B. Basavaraj, D. Navami, N. H. Deepthi, M. Venkataravanappa, R. Lokesh, K. H. Sudheer Kumar and T. K. Sreelakshmi, *Inorg. Chem. Commun.*, 2020, **120**, 108164.
39. P. J. King, M. Werner, P. R. Chalker, A. C. Jones, H. C. Aspinall, J. Basca, J. S. Wrench, K. Black, H. O. Davies and P. N. Heys, *Thin Solid Films*, 2011, **519**, 4192-4195.
40. A. El-Habib, M. Addou, A. Aouni, J. Zimou, M. Diani, H. Ftouhi and Z. E. Jouad, *Surfaces and Interfaces*, 2021, **23**, 100906.
41. E. Mamontov, T. Egami, R. Brezny, M. Koranne and S. Tyagi, *J. Phys. Chem. B*, 2000, **104**, 11110-11116.
42. A. K. Pal, S. Som and C.-H. Lu, *Ceram. Int.*, 2018, **44**, 18256-18263.
43. D. Samson Daniel, S. Ernest and S. Fairose, *Mater. Today*, 2021, **38**, 2885-2889.
44. B. Bao, Y. Sun, X. Li, L. Li and Y. Yu, *FlatChem*, 2023, **39**, 100494.
45. S. Babu, J.-H. Cho, J. M. Dowding, E. Heckert, C. Komanski, S. Das, J. Colon, C. H. Baker, M. Bass, W. T. Self and S. Seal, *Chem. Commun.*, 2010, **46**, 6915-6917.
46. K. Kumari, R. N. Aljawfi, A. K. Chawla, R. Kumar, P. A. Alvi, A. Alshoaibi, A. Vij, F. Ahmed, M. Abu-samak and S. Kumar, *Ceram. Inter.*, 2020, **46**, 7482-7488.
47. D. Park, M. Kim, K. Beom, S.-Y. Cho, C. J. Kang and T.-S. Yoon, *J. Alloys Compd*, 2019, **786**, 655-661.
48. T. T. Be Lan, Y.-T. Li, A.-C. Aidan Sun, H.-C. Lu and S.-F. Wang, *Mater. Sci. Semicond. Process.*, 2022, **137**, 106177.
49. A. G. Khairnar and A. M. Mahajan, *Bull. Mater. Sci.*, 2013, **36**, 259-263.
50. J.-G. Yu, B. C. Yang, J. W. Shin, S. Lee, S. Oh, J.-H. Choi, J. Jeong, W. Noh and J. An, *Ceram. Int.*, 2019, **45**, 3811-3815.
51. I. Y. Habib, J. Burhan, F. Jaladi, C. M. Lim, A. Usman, N. T. R. N. Kumara, S. C. E. Tsang and A. H. Mahadi, *Catal. Today*, 2021, **375**, 506-513.
52. S. Xie, Z. Wang, F. Cheng, P. Zhang, W. Mai and Y. Tong, *Nano Energy*, 2017, **34**, 313-337.
53. M. Kurian, *J. Environ. Chem. Eng.*, 2020, **8**, 104439.
54. D. Schweke, Y. Mordehovitz, M. Halabi, L. Shelly and S. Hayun, *Adv. Mater.*, 2018, **30**, 1706300.
55. R. Takada and H. Yao, *Chem. Phys. Lett.*, 2023, **825**, 140586.
56. M. F. Al-Kuhaili, S. M. A. Durrani and I. A. Bakhtiari, *Appl. Surf. Sci.*, 2008, **255**, 3033-3039.
57. B. K. Nath, C. Chaliha, E. Kalita and M. C. Kalita, *Carbohydr. Polym.*, 2016, **148**, 397-405.
58. R. Mueen, A. Morlando, H. Qutaish, M. Lerch, Z. Cheng and K. Konstantinov, *J. Mater. Sci.*, 2020, **55**, 6834-6847.
59. R. Meng, X. Feng, Y. Yang, X. Lv, J. Cao and Y. Tang, *ACS Appl. Mater. Interfaces*, 2019, **11**, 13273-13278.

60. T. Hu, S. Xiao, H. Yang, L. Chen and Y. Chen, *Chem. Commun.*, 2018, **54**, 471-474.
61. R. Fang, S. Wu, W. Chen, Z. Liu, S. Zhang, R. Chen, Y. Yue, L. Deng, Y.-B. Cheng, L. Han and W. Chen, *ACS Nano*, 2018, **12**, 2403-2414.
62. Z. Xing, S.-H. Li, B.-S. Wu, X. Wang, L.-Y. Wang, T. Wang, H.-R. Liu, M.-L. Zhang, D.-Q. Yun, L.-L. Deng, S.-Y. Xie, R.-B. Huang and L.-S. Zheng, *J. Power Sources*, 2018, **389**, 13-19.
63. R. Pandey, A. P. Saini and R. Chaujar, *Vacuum*, 2019, **159**, 173-181.
64. J. Yang, J. Xu, Q. Zhang, Z. Xue, H. Liu, R. Qin, H. Zhai and M. Yuan, *RSC Adv.*, 2020, **10**, 18608-18613.
65. A. Pang, J. Li, X.-F. Wei, Z.-W. Ruan, M. Yang and Z.-N. Chen, *Nanoscale Adv.*, 2020, **2**, 4062-4069.
66. X. Wang, L.-L. Deng, L.-Y. Wang, S.-M. Dai, Z. Xing, X.-X. Zhan, X.-Z. Lu, S.-Y. Xie, R.-B. Huang and L.-S. Zheng, *J. Mater. Chem. A*, 2017, **5**, 1706-1712.
67. S. Ahmmed, A. Aktar, M. H. Rahman, J. Hossain and A. B. M. Ismail, *Semicond. Sci. Technol.*, 2021, **36**, 035002.
68. L. Zhang, Z. Che, J. Shang, Q. Wang, M. Cao, Y. Zhou, Y. Zhou and F. Liu, *ACS Appl. Mater. Interfaces*, 2023, **15**, 10838-10846.
69. N. S. Arul, Y. H. Lee, D. U. Lee and T. W. Kim, *J Nanosci. Nanotechnol*, 2015, **15**, 232-235.
70. M. T. Dang, L. Hirsch and G. Wantz, *Adv. Mater.*, 2011, **23**, 3597-3602.
71. M. S. Bhuiyan, M. Paranthaman and K. Salama, *Supercond. Sci. Tech.*, 2006, **19**, R1.
72. U. Vongsaysy, B. Pavageau, G. Wantz, D. M. Bassani, L. Servant and H. Aziz, *Adv. Energy Mater.*, 2014, **4**, 1300752.
73. A. Cravino, P. Schilinsky and C. J. Brabec, *Adv. Funct. Mater.*, 2007, **17**, 3906-3910.
74. A. Pereira, M. Blouin, A. Pillonnet and D. Guay, *Mater. Res. Expres*, 2014, **1**, 015704.
75. S. A. A R Sayyed, N. I. Beedri, V. S. Kadam and H. M. Pathan, *Bull. Mater. Sci.*, 2016, **39**, 1381-1387.
76. P. Burroughs, A. Hamnett, A. F. Orchard and G. Thornton, *J. Chem. Soc., Dalton Trans.*, 1976, DOI: 10.1039/DT9760001686, 1686-1698.
77. F. ç. Larachi, J. Pierre, A. Adnot and A. Bernis, *Appl. Surf. Sci.*, 2002, **195**, 236-250.
78. A. Pfau and K. D. Schierbaum, *Surf. Sci.*, 1994, **321**, 71-80.
79. C. Wang, Z. Wu, G. Liu, S. Bai, L. Guo, L. He and Y.-F. Song, *Inorg. Chem. Front.*, 2022, **9**, 5926-5931.
80. H. Wang, X. Zhang, Z. Su and T. Chen, *Langmuir*, 2023, **39**, 18366-18379.
81. Y. Zhu, X. Sun, R. Zhang, X. Feng and Y. Zhu, *Small*, 2024, **20**, 2400191.
82. H. Noma, Y. Miwa, I. Yokoyama and K. Machida, *J. Mol. Struct.*, 1991, **242**, 207-219.
83. T. Mokkelbost, I. Kaus, T. Grande and M.-A. Einarsrud, *Chem. Mater.*, 2004, **16**, 5489-5494.
84. R. Ganesamoorthy, G. Sathiyan and P. Sakthivel, *Sol. Energy Mater. Sol. Cells*, 2017, **161**, 102-148.
85. T. Erb, U. Zhokhavets, G. Gobsch, S. Raleva, B. Stühn, P. Schilinsky, C. Waldauf and C. J. Brabec, *Adv. Funct. Mater.*, 2005, **15**, 1193-1196.
86. W. Ma, C. Yang, X. Gong, K. Lee and A. J. Heeger, *Adv. Funct. Mater.*, 2005, **15**, 1617-1622.
87. J. Bertrandie, J. Han, C. S. P. De Castro, E. Yengel, J. Gorenflot, T. Anthopoulos, F. Laquai, A. Sharma and D. Baran, *Adv. Mater.*, 2022, **34**, 2202575.
88. K. Oura, H. Wada, M. Koyama, T. Maemoto and S. Sasa, *J. Inf. Disp.*, 2022, **23**, 105-113.
89. J. Chen, X. Zhou, X. Liu, Q. Luo, K. Feng and Y. Zhou, *Solar RRL*, 2024, **8**, 2400164.
90. A. T. Vai, V. L. Kuznetsov, J. R. Dilworth and P. P. Edwards, *J. Mater. Chem. C*, 2014, **2**, 9643-9652.